A&A 637, A54 (2020)
https://doi.org/10.1051/0004-6361/202037823

Astronomy & Astrophysics

The second *u*-band extension of the WINGS cluster survey[⋆,⋆⋆]

M. D'Onofrio[1,3], A. Grado[2], D. Bettoni[3], J. Fritz[4], M. Gullieuszik[3], A. Moretti[3], A. Omizzolo[5,3], and B. M. Poggianti[3]

[1] Department of Physics and Astronomy, University of Padua, Vicolo Osservatorio 3, 35122 Padua, Italy
e-mail: mauro.donofrio@unipd.it
[2] INAF – Capodimonte Astronomical Observatory, Salita Moiariello 16, 80131 Naples, Italy
[3] INAF – Padua Astronomical Observatory, Vicolo Osservatorio 5, 35122 Padua, Italy
[4] Instituto de Radio astronomía y Astrofísica, UNAM, Morelia, Michoacán, Mexico
[5] Specola Vaticana, 00120 Vatican City, Italy

Received 26 February 2020 / Accepted 25 March 2020

ABSTRACT

Context. This is the second *u*-band extension of the WIde-field Nearby Galaxy-cluster Survey (WINGS) whereby 39 clusters were imaged with the ESO-VLT survey telescope. This follows the first part of the survey which was performed with several telescopes of the northern hemisphere in the *U* Cousin–Bessel filter band covering 17 clusters.
Aims. The *u*-band data, in combination with those already collected by the WINGS survey, permit a detailed multi-wavelength investigation of the properties of the member galaxies from the cluster center out to the periphery.
Methods. We used SExtractor to derive the main properties of the galaxies in the observed fields and measure the $u - V$ colors on circular apertures of increasing radius. The photometric accuracy of the magnitudes was calibrated with the standard stars and was tested by means of comparisons with the *u*-band data of the Sloan Digital Sky Survey (SDSS).
Results. We present the catalogs of the photometric analysis performed by SExtractor. We also provide a brief analysis of the $u - V$ versus V color–magnitude diagram of our clusters, the plots of the color as a function of the cluster-centric distance (for cluster members only), the mass–color relation and the correlation of the current star formation rate (SFR) with the absolute V and u magnitudes for the galaxies in the observed fields.

Key words. galaxies: clusters: general – galaxies: photometry – galaxies: evolution

1. Introduction

Recent years have seen the acquisition of an enormous amount of photometric and spectroscopic data coming from large sky surveys. Most of these data cover the optical bands while the *u*-band has mostly been neglected. The main problems encountered with this band come from the intrinsic faintness of sources, with the spectral energy distribution (SED) of galaxies displaying a peak at longer wavelengths. This typically means that *u*-band observations are more expensive in terms of telescope time.

Nevertheless, the *u*-band contains very important astrophysical information. For example, the *u*-band is useful for measuring metallicity; the young and hot stellar populations have their greatest contrast in the *UV*, making this band important for studying star-formation in the nearby Universe; and for more distant galaxies the *u*-band is very useful for the determination of photometric redshifts. The *u*-band data are believed to be more sensitive to the recent star formation activity of galaxies than any other broadband filter (Kennicutt 1998a; Barbaro & Poggianti 1997). In addition, the spatial color information within galaxies can greatly help to distinguish between various physical processes that have influenced the star formation history. In particular, we hope to reveal the role played by ram pressure stripping, by shock-induced star formation events, by starbursts driven by tidal encounters, and so on. These observations are also expected to establish the correlation between galaxy morphology (from the *V*-band imaging), mass (from *K*-band data and spectra), and the *u*-band properties of galaxies.

With this paper we want to enlarge the *u*-band database by presenting the photometry of galaxies in 39 out of 76 clusters observed by OmegaCam at the ESO-VST telescope. These observations represent the second extension in the *u*-band of the WINGS and Omega-WINGS surveys (Fasano et al. 2006; Varela et al. 2009; Gullieuszik et al. 2015). The first *U*-band extension was realized by Omizzolo et al. (2014) who observed 17 clusters with three different wide-field cameras using the Cousin/Bessel *U* band: (i) the 90′ camera at the 90″ BOK telescope (Kitt Peak); (ii) the Wide Field Camera at the 2.5 m *Isaac Newton* Telescope (WFC at INT); and (iii) the Large Binocular Camera at the Large Binocular Telescope (LBC at LBT). Another cluster, Abell 970, was studied using the *U*-band images taken with WFI at the MPG/ESO-2.2 m telescope in La Silla (Chile).

This second *u*-band survey will allow the detailed study of the 2D maps of the current star formation activity for a significant sample of galaxies, not only in the central region covered by the fibers of the spectrographs (1.6−2.6 arcsec), but also in the outer parts, taking advantage of the multi-waveband images now available.

WINGS and Omega-WINGS are two large optical sky surveys dedicated to the study of the properties of galaxies in nearby clusters ($0 < z < 0.07$). WINGS mapped 76 clusters in the *B*

⋆ Full Table A.1 is only available at the CDS via anonymous ftp to cdsarc.u-strasbg.fr (130.79.128.5) or via http://cdsarc.u-strasbg.fr/viz-bin/cat/J/A+A/637/A54
⋆⋆ Based on observations collected at the European Southern Observatory under ESO GTO programs IDs (089.B-0683-098.B-0657).

and V bands with the Wide Field Camera (WFC, $34' \times 34'$) of the INT-2.5m telescope in La Palma (Canary Islands, Spain) and with the Wide Field Imager (WFI, $34' \times 33'$) of the MPG/ESO-2.2 m telescope in La Silla (Chile), while Omega-WINGS used OmegaCam (1 deg^2 field), the camera of the VLT Survey Telescope (VST), to map 57 out of 76 clusters in the same bands. Both surveys are ∼90% complete at $V \sim 21.7$.

The near-infrared (NIR) extension WINGS-NIR (Valentinuzzi et al. 2009) saw the mapping of a subsample of 28 clusters in the J and K bands with the WFCAM camera mounted at the UKIRT telescope. Each mosaic is ≈0.79 deg^2 and the 90% detection rate limits for the galaxies reached $J = 20.5$ and $K = 19.4$.

Two spectroscopic follow-up observations have also been realized: the first includes a subsample of 48 clusters (26 in the northern hemisphere and 22 in the southern hemisphere) observed with WYFFOS at the WHT telescope in La Palma ($\Delta\lambda = 3800 \div 7000$ Å, spectral resolution full width half maximum ($FWHM$) = 3 Å) and with the Two degree Field (2dF) spectrograph at the Anglo Australian telescope (AAT; λrange = 3600 ÷ 8000 Å, spectral resolution $FWHM = 6$ Å). The second used the AAOmega spectrograph at the AAT (resolution $R = 1300$, $FWHM = 3.5 \div 6$ Å) in the wavelength range 3800÷9000 Å (Moretti et al. 2017). The sample magnitude completeness is 80% at $V = 20$. The spectroscopic data permitted the measurement of the redshift of thousands of galaxies, together with their cluster membership (Cava et al. 2009; Moretti et al. 2017), and the determination of their star formation history (SFH) from the SED (Fritz et al. 2007, 2011).

For both the WINGS and Omega-WINGS samples, Fasano et al. (2012) derived the morphological types of the galaxies with the program MORPHOT. This tool provides an automatic morphological classification based on 21 diagnostic parameters directly derived from the galaxy images, giving two independent classifications: one based on a maximum likelihood semi-analytical technique and one on a neural network machine.

The paper is organized as follows: in Sect. 2 we present the data sample including the information on the VST runs; in Sect. 2.1 we describe the steps of the data reduction and provide the parameters of the photometric calibration procedure; in Sect. 3 we give the details of the `SExtractor` (Bertin & Arnouts 1996) analysis performed on the final calibrated images; in Sect. 4 we discuss the $u - V$ versus V color–magnitude (c–m) diagrams, the plots of the color distribution against the distance from the cluster center, the mass–color relation and the plots of the current star formation rate (SFR) versus the absolute magnitude of our galaxies in the u and V-bands; finally in Sect. 5 we provide our conclusions. The appendix contains an example of the tables that we have uploaded at the Centre de Données Astronomiques (CDS) de Strasbourg (Table A.1), the table with the coefficients of the fits of the red sequence visible in the c–m relations (Table A.2) and the tables with the coefficients of the fits of the log(SFR)−M relations (Table A.3).

2. The data sample

These data are part of the OmegaCam guaranteed time observations (GTO), from P89 to P98, obtained by the WINGS team at the ESO-VST survey telescope. With three exposures of 20 min each, 39 WINGS clusters were imaged in the u-band filter.

The list of the observed clusters is shown in Table 1. The first and second columns give the name of the WINGS cluster and the ESO period of observation. The third and fourth columns report the quality grade of the observing night condition and the date of observation. In total, 26 clusters were observed under grade A, 11 under grade B, 2 under grade C, and 7 under grade D. The CCD images were reduced (see Sect. 2.1) and later analyzed using `SExtractor` (see Sect. 3).

Table 1. Clusters observed in the u-band survey.

Cluster	ESO period	Grade	Date
A1644	P89	A	16/04/2012
A119	P89	A	24/07/2012
A85	P90	D	08/10/2012
A2399	P90	A	09/10/2012
A133	P90	A	09/10/2012
A500	P90	B	12/12/2012
A3395	P90	B	11/01/2013
A1631a	P90	A	19/02/2013
A1736	P90	D	17/03/2013
A1983	P91	D	11/04/2013
MKW3s	P91	D	11/04/2013
A3556	P91	D	12/04/2013
A3560	P91	D	12/04/2013
A2382	P91	B	05/06/2013
A2399	P91	A	06/06/2013
A3809	P91	A	06/06/2013
A2457	P91	A	02/08/2013
A160	P92	C	31/10/2013
A3266	P92	A	05/11/2013
A3395	P92	A	12/11/2013
A3376	P92	A	30/12/2013
A3490	P92	B	01/03/2014
A3716	P93	C	03/07/2014
A3667	P93	B	25/07/2014
A2399	P93	A	23/08/2014
A2415	P93	A	23/09/2014
A3716	P93	B	24/09/2014
A970	P94	A	18/01/2015
A1069	P94	A	24/02/2015
A548b	P96	A	14/11/2015
A3128	P96	A	15/11/2015
A500	P96	D	15/11/2015
A754	P96	A	15/11/2015
A780	P96	A	13/12/2015
A957	P96	A	10/02/2016
A970	P96	A	15/02/2016
A3880	P97	B	11/07/2016
IIZW108	P97	B	11/07/2016
A4059	P97	B	12/07/2016
A85	P97	A	12/07/2016
A168	P98	A	06/10/2016
A147	P98	B	06/10/2016
A3158	P98	B	09/10/2016
A3164	P98	A	07/11/2016
A3528a	P98	A	22/03/2017
A3528b	P98	A	27/03/2017

Notes. Columns 1–4 provide the cluster name, the ESO observing period, the grade quality of the exposure, and the date of observation.

2.1. The photometric and astrometric calibration

The u-band imaging mosaics were produced with the VST-Tube pipeline (Grado et al. 2012) developed to process wide field

Table 2. Results of the data analysis.

Cluster	*FWHM* (arcsec)	Zero point	Color term
A85	1.11	23.224 ± 0.006	0.019 ± 0.016
A119	0.76	23.319 ± 0.006	0.026 ± 0.016
A133	0.90	23.295 ± 0.006	0.019 ± 0.016
A147	1.10	23.238 ± 0.008	0.013 ± 0.003
A160	1.10	23.190 ± 0.006	0.032 ± 0.016
A168	0.90	23.238 ± 0.008	0.013 ± 0.003
A500	0.97	23.279 ± 0.006	0.019 ± 0.016
A548b	0.72	23.263 ± 0.008	0.063 ± 0.002
A754	0.65	22.143 ± 0.081	0.030 ± 0.003
A780	1.00	22.124 ± 0.069	0.030 ± 0.003
A957	1.16	22.023 ± 0.093	0.030 ± 0.003
A970	1.10	23.175 ± 0.007	0.045 ± 0.004
A1069	1.00	23.189 ± 0.004	0.057 ± 0.003
A1631a	1.05	23.231 ± 0.006	0.019 ± 0.016
A1644	0.85	23.274 ± 0.006	0.016 ± 0.016
A1736	1.18	23.293 ± 0.006	0.023 ± 0.016
A1983	1.70	23.313 ± 0.006	0.028 ± 0.016
A2382	1.10	23.291 ± 0.006	0.035 ± 0.016
A2399	1.00	23.265 ± 0.015	0.033 ± 0.010
A2415	0.98	23.303 ± 0.093	0.030 ± 0.010
A2457	1.00	23.300 ± 0.006	−0.003 ± 0.016
A3128	1.15	23.211 ± 0.004	0.053 ± 0.017
A3158	1.10	23.098 ± 0.005	0.046 ± 0.002
A3164	0.91	23.115 ± 0.004	0.047 ± 0.002
A3266	1.01	23.064 ± 0.006	0.063 ± 0.016
A3376	1.05	23.391 ± 0.010	0.030 ± 0.003
A3395	1.00	23.239 ± 0.006	0.019 ± 0.016
A3490	1.20	23.154 ± 0.008	0.068 ± 0.003
A3528a	1.13	23.230 ± 0.005	0.030 ± 0.001
A3528b	0.94	23.013 ± 0.004	0.055 ± 0.002
A3556	1.50	23.186 ± 0.006	0.027 ± 0.016
A3560	1.35	23.186 ± 0.008	0.027 ± 0.016
A3667	0.85	23.309 ± 0.015	0.019 ± 0.010
A3716	1.55	23.216 ± 0.007	0.009 ± 0.005
A3809	0.90	23.265 ± 0.006	0.033 ± 0.016
A3880	1.09	23.269 ± 0.006	0.003 ± 0.003
A4059	1.50	23.264 ± 0.008	−0.007 ± 0.004
IIZW108	1.15	23.269 ± 0.006	0.003 ± 0.003
MKW3s	1.00	23.313 ± 0.006	0.028 ± 0.016

Notes. Columns 1–4 provide the cluster name, the mean FWHM of the image, the zero point of the calibration, and the color term slope of the color equation.

images. The input of the pipeline are the science and calibration exposures acquired by the optical camera, and the instrument and configuration files. Through a graphical user interface it is possible to choose among different reduction algorithms and processing strategies. The output are the fully astrometrically and photometrically calibrated co-added image mosaics, their weight and flag maps, and the catalogs of the extracted sources with aperture and point spread function (PSF) photometry.

Once the raw images are downloaded from the ESO archive, the pipeline performs a first quality check. The images are overscan corrected and the master calibration files are produced. These consist in the master bias, which is a sigma-clipped combination of typically ten bias exposures, and a master flat-field obtained by properly combining twilight and science images. The use of both twilight and science images for the high-frequency and low-frequency spatial variations, respectively, ensures correction of the gain variations at the level of a few percent. It is worth noting that to process images of a particular night, the science images necessary to create the master flat-field should ideally be chosen from the same night being processed, with the same exposure time, and such that they do not contain bright and/or extended sources.

Wide-field high-resolution images are typically affected by two drawbacks: the camera is made of a mosaic of CCDs; and diffuse light entering the telescope contributes additively causing what is referred to as the "illumination effect". The first drawback requires the equalization of the CCD gains in order to obtain a unique zero-point for the whole mosaic, while the second requires an illumination correction, i.e., observing photometric fields (typically equatorial Landolt stars fields Landolt 1992) to map the zero-point variation as a function of position. All these procedures are executed by the VST-Tube pipeline in order to remove as many of the instrumental signatures from the images as possible.

The images are then astrometrically calibrated against the 2MASS reference catalog (Skrutskie et al. 2006) using Scamp (Bertin 2006). Scamp also provides the relative photometric corrections among dithered exposures minimizing the flux differences among overlapping sources (see Capaccioli et al. 2015, for more details).

For the photometric calibration, we used the ESO calibration plan[1] for Omegacam, which foresees observations of equatorial Landolt star fields spanning wide airmass ranges. When available, these fields are used for the absolute photometric calibration using the Data Release 11 (DR11) of the SDSS catalog (Alam et al. 2015) as a reference. The differences between the reference catalog and the instrumental magnitudes are used to fit the zero point, extinction coefficient, and color term. The final mosaic image is scaled so that the final calibrated magnitude equation in the u SDSS system is:

$$u[\mathrm{SDSS}] = u[\mathrm{VST}] + \mathrm{Z.P.} + \mathrm{C.T.}(u - g), \quad (1)$$

where C.T. is the color term provided in Table 2 and Z.P. is the zero point of the calibration. The images were successively re-scaled in order to have a zero point of 30 for all mosaics.

The zero point is relative to an aperture diameter of 4 arcsec. The absolute photometric calibration of the VST images is done by comparing the PSF magnitudes of SDSS with the 4 arcsec aperture magnitudes of the VST for the standard fields. This aperture contains all the flux of the stars and there is no need to make opening corrections. The choice of such a large aperture, which has the disadvantage of introducing more noise, is that the resulting photometry is insensitive to seeing variations.

The absolute photometric calibration is performed by comparing the standard stars observed in the night with the reference photometric standard stars. Figure 1 shows an example of the output of the absolute photometric calibration for the cluster A119.

Table 2 summarizes the results of the calibration procedure. Column 1 gives the name of the cluster, Col. 2 the average FWHM of the mosaic image, Col. 3 the zero point derived from the fit of the $M - m$ (u[SDSS]−u[VST]) versus $(u - g)$ distribution of the observed standard stars (see Fig. 1), and Col. 4 the relative color term (C.T.). It should be noted that the accuracy of the zero point is only the formal uncertainty associated to the fit;

[1] www.eso.org/sci/facilities/paranal/instruments/omegacam/doc.html

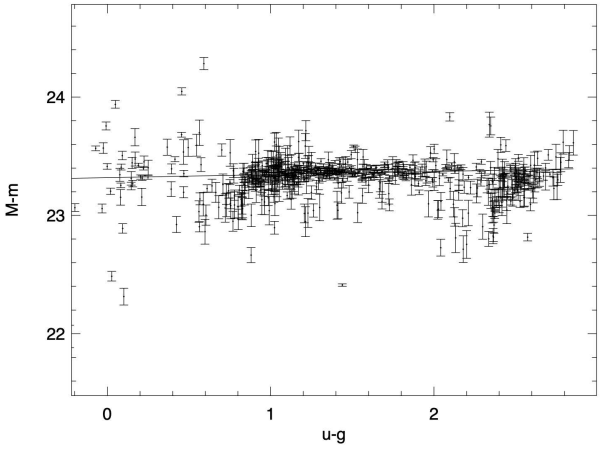

Fig. 1. Calibration of the photometry for the cluster A119. The difference between the SDSS and VST u-band magnitudes is plotted against the $(u - g)$ color of standard stars.

it does not represent the real accuracy of the photometric zero-point calibration. Our estimate is that a 0.1 mag uncertainty is very plausible, as can be seen from Fig. 2, which shows a direct comparison of the VST and SDSS u-band data for 3421 stars in the fields of the clusters in common between the two datasets. The red dots in the figure mark the average values in different bins of magnitudes and the relative uncertainty. Magnitudes obtained with VST photometry are on average ∼0.1 mag fainter than those from SDSS up to $u \sim 23$ mag. Above this threshold, the SDSS data are progressively more uncertain (the DR12 completeness is in fact 95% at $u \sim 22$ for unresolved stars). In addition, the SDSS sample does not include objects with magnitudes fainter than $u = 25$.

Figure 3 shows a direct comparison of the VST and SDSS u-band data using a different circular aperture for the VST images in the `SExtractor` analysis. In particular, here we used a diameter of 10 pixels (that with the scale of 0.213 arcsec pixel^{-1} is approximately equal to 2 arcsec). We note that now the VST magnitudes are systematically fainter than those of SDSS.

In the last step of the processing, which makes use of the software Swarp (Bertin et al. 2002), the images are co-added using a weighted average. Each final co-added image has an associated weight map and flag map. The weight map is an inverse variance map that takes into account contributions from the flat-field, illumination correction, CCD gain equalization, flux scaling, cosmic rays, and bad pixels. The flag map contains the number of pixels that contribute to the final mosaic; it takes into account the number of input images, the bad pixels, the mask of the cosmic rays, and the masks of halos and spikes of bright stars produced by a dedicated procedure in VST-tube.

Now we compare our photometry with that already available in the Cousin/Bessel U band from Omizzolo et al. (2014). The cluster in common with the previous U band extension are A119, A970, A1983, and A2399. Figure 4 shows a one-to-one comparison between photometry in the two bands for cluster A119. The black dots mark the total magnitudes obtained by `SExtractor` for the galaxies that are in common between the two datasets; their are 739 in total. The thick solid line gives the best fit obtained by rejecting the points that are too far from the main distribution, while the thin line is the one-to-one equal line. We obtain:

$$u[\mathrm{BOK}] = 1.05\, u[\mathrm{VST}] - 1.73, \quad (2)$$

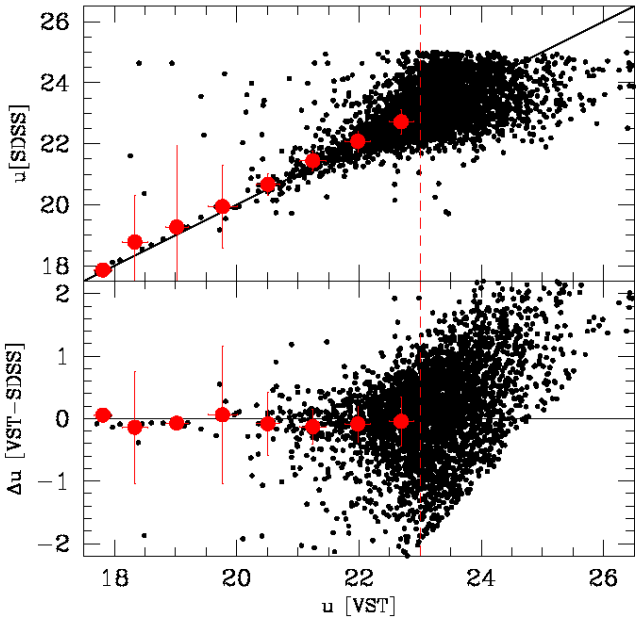

Fig. 2. Comparison between the u magnitudes of SDSS and our VST data for the star sample. We note that the SDSS sample does not include objects with magnitudes fainter than $u = 25$ and is progressively incomplete for $u \geq 23.0$. The red dashed lines in both diagrams give the limit of completeness of the SDSS.

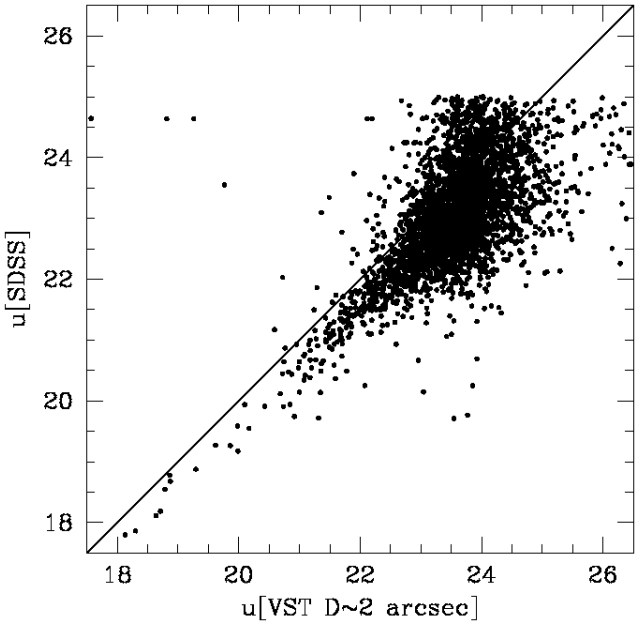

Fig. 3. Comparison between the u magnitudes of SDSS and our VST data for the star sample using a different aperture for the photometry of the VST data.

with a c.c. = 0.99 and a rms = 0.19. We also reiterate that the u (U) photometric band peaks at 3500 Å (3600 Å) and spans an interval of 60 Å (70 Å). The two sets of magnitudes therefore differ by approximately ∼0.6–0.7 mag[2].

[2] The most correct transformation depends on the color of the systems. See: http://www.sdss3.org/dr8/algorithms/sdssUBVRITransform.php

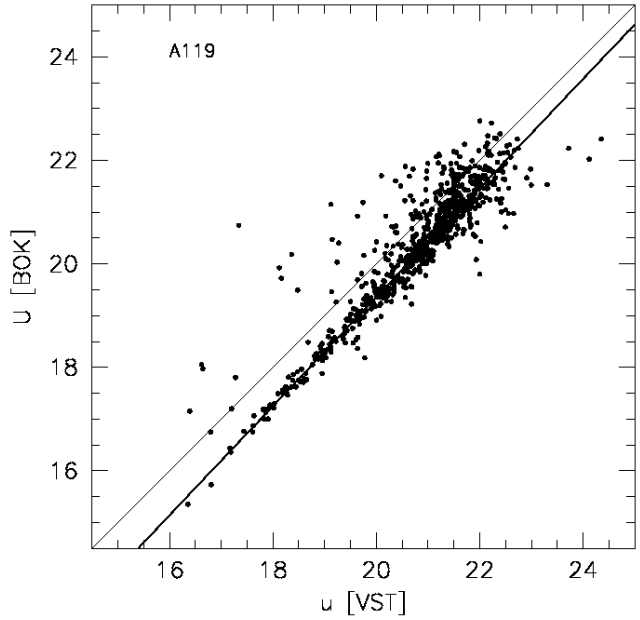

Fig. 4. Direct comparison between the U-band photometry of the BOK and that of the VST telescopes for cluster A119.

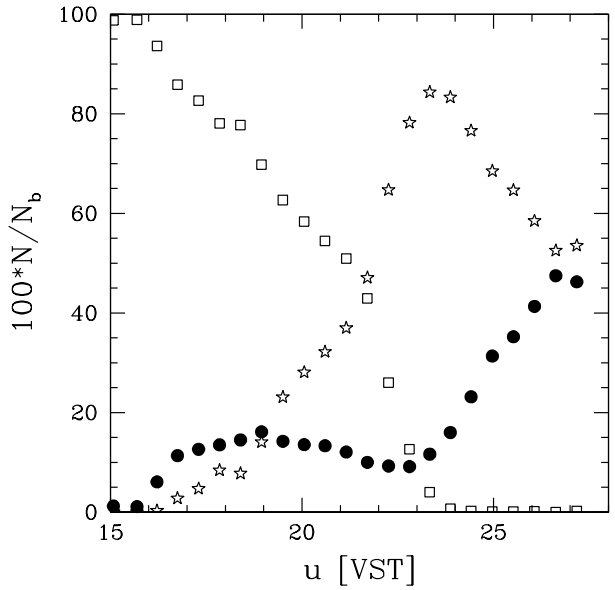

Fig. 5. Fraction of galaxies (black filled circles), stars (open squares), and unknown objects (open stars) per bin of magnitude coming from the CLASS_STAR index of five clusters observed under good seeing conditions.

3. The SExtractor analysis

The source extraction and the measurement of the photometric and structural parameters of our galaxies were then obtained using SExtractor (Bertin & Arnouts 1996) on the final mosaic image of each cluster. SExtractor provided the circular aperture magnitudes around the center of each galaxy as well as many other parameters, which we list below.

SExtractor was used in dual mode for 32 clusters, using the V-band images of the VST survey (Gullieuszik et al. 2015) as reference, and in single mode for 7 clusters (A133, A548b, A780, A1644, A1736, A3164 and A3490) not observed in the V-band by Omega-WINGS. The dual mode uses the coordinates of the objects detected in the V band and performs the photometry in the u-band only for these objects. We nevertheless verified that the normal and dual mode produce identical results.

We estimated the local background on a box size of 64 pixels adopting a detection threshold of 1.5σ above the background. For the photometry, we used circled apertures with diameters of 5, 10, 15, and 20 pixels, 1.60, 2.00, and 2.16 arcsec (transformed in pixels), and 2, 5, and 10 kpc (also transformed in pixels). The adopted pixel scale size of the camera was 0.213 arcsec. For the latter three values we used the kpc arcsec^{-1} scales listed in the WINGS database Moretti et al. (2014). For the final classification of the sources (galaxies/stars/unknown objects) we adopted those given by Gullieuszik et al. (2015) for the V-band data that have already been tested on many occasions. For the clusters not observed in the V-band, we used the CLASS_STAR index provided by SExtractor. However, we note that in some cases the two classifications do not agree; this occurs when objects are very faint.

Figure 5 shows the fraction of galaxies, stars, and unknown objects in each bin of magnitude obtained from the analysis of five clusters observed under good seeing conditions. We note that the fraction of unknown objects is equal to the fraction of galaxies at $u \sim 19$. At this magnitude, we have approximately 60% stars and 15% galaxies. At $u \sim 23$, the number of objects detected as galaxies decreases to ~10%, while the unknown fraction reaches a maximum. For magnitudes fainter than $u \sim 25$ all objects are classified as unknown.

The final list of parameters that can be found in the published catalogs is the following:
WINGS_ID: WINGS identification name (when available);
CLUSTER: cluster name;
RA, DEC: equatorial coordinates of the barycentre of the source;
X_PEAK, Y_PEAK: coordinates on the peak of flux in the object image, in pixels;
MAG_ISO: isophotal magnitude, defined using the detection threshold as the lowest isophote;
MAG_ISOCOR: isophotal magnitude corrected to retrieve the fraction of flux lost by isophotal magnitudes by assuming Gaussian intensity profiles;
MAG_AUTO: Kron-like aperture magnitude. This is the most precise estimate of total magnitudes for galaxies;
MAG_APER: the aperture magnitudes;
MU_MAX: surface brightness of the brightest pixel in mag arcsec^{-2};
KRON_RADIUS: Kron radius in pixels;
ISOAREA_IMAGE: isophotal area in pixels;
A_IMAGE,B_IMAGE: semi-major and semi-minor axes in pixels. These were used to compute the galaxy flattening b/a;
ELONGATION: ratio of A_IMAGE/B_IMAGE;
THETA_IMAGE: position angle with respect to the north and measured counter-clockwise;
FWHM_IMAGE: full width at half maximum in arcseconds;
CLASS_STAR: stellarity index derived for the u-band, providing an initial idea of the source morphology (stars, galaxies or unknown objects);
CLASS: final object classification according to Gullieuszik et al. (2015) (when available).

Figure 6 shows a one-to-one comparison of the u-band total magnitudes of our galaxies with the values tabulated by the SDSS in the DR12. We have only 12 clusters in common with SDSS. We note that the scatter increases significantly after $u >$ 21 mag. This is due to a number of factors, such as the low S/N, difficulties encountered by SExtractor in defining the galaxy extension, errors in the deblending routine, the proximity of

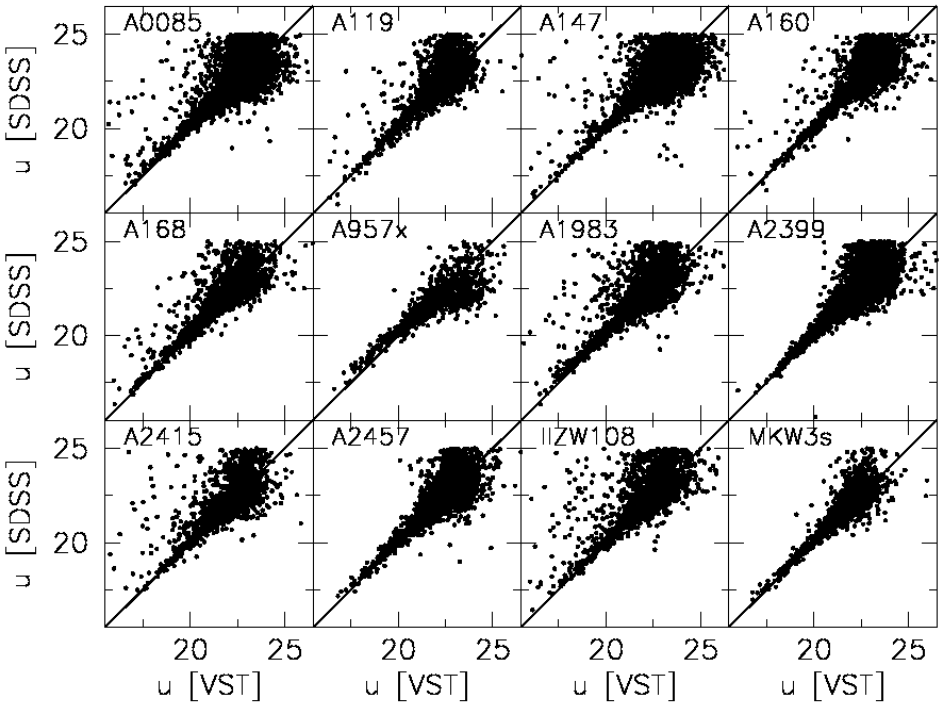

Fig. 6. Direct comparison between the u magnitudes of galaxies in the SDSS database and our VST data. We note the large increase in scatter for magnitudes fainter than $u \sim 21$.

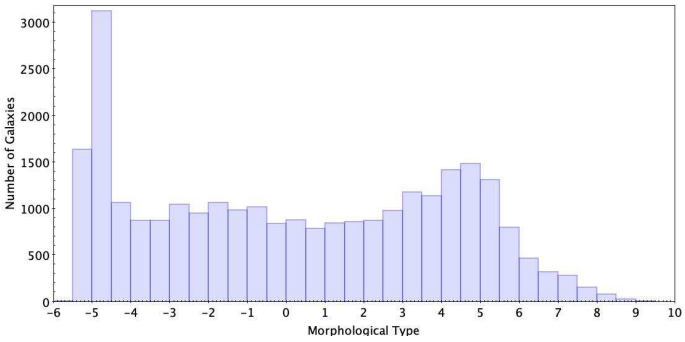

Fig. 7. Morphological types of 27215 galaxies in the fields of our clusters derived by the MORPHOT analysis.

bright objects, and so on. The objects fainter than $u \sim 22$ have a larger uncertainty in both surveys. However, the good level of our calibration is ultimately confirmed by this comparison. The total u-magnitudes of our galaxies have an average scatter of ∼0.1−0.2 mag below $u = 21.0$ with respect to the SDSS data.

The total number of galaxies of all clusters for which both V and u-band photometry are available is 67 825. By matching these with the MORPHOT catalog of Fasano et al. (2012) we obtain 27 215 objects. Figure 7 shows the histogram of the morphological types T of these galaxies. We note that all morphological types are present in our sample, but elliptical galaxies ($T = -5$) and late spiral galaxies ($T = 3 \div 6$) are more frequent.

4. Brief examples of data exploitation

Here, we provide some preliminary examples of the scientific exploitation of the u-band data, in particular when combined with those already available from the WINGS database. In the sections below we provide the $u - V$ versus M_V color magnitude diagrams of our clusters, the plots of the galaxy color versus the distance from the center of the clusters, the trends observed between the u and V luminosities, and the current star formation rate derived from the spectroscopic WINGS extension.

4.1. The u-V color of cluster galaxies

The color–magnitude diagram (CMD) is one of the main diagnostic tools used to understand the physical properties of stars and galaxies, and, in recent years, also of clusters of galaxies (Cariddi et al. 2018). Color–magnitude diagrams have allowed researchers to infer the past history of galaxies and clusters and have been considered to be key cosmological probes for a long time now (Tully et al. 1982; Bower et al. 1992). In particular, the scatter of the red sequence seen in the CMD places constraints on the age spread of the stellar population, while its slope provides indications on the merger history of the cluster (Bower et al. 1998). Understanding the origin of the red sequence and its slope and scatter width has been the aim of many studies (see for more details Sciarratta et al. 2019). The most commonly accepted view today is that the red sequence is a metallicity sequence and not an age sequence; however, the age dispersion seems to increase with decreasing galaxy mass. The problem of reproducing the characteristics of the CMD remains unsolved, meaning that data of this kind are very useful. In such a context, the CMD obtained with the u-band data is important for deciphering the contribution of the young and hot stellar population in galaxies.

The $u - V$ versus M_V CMDs of our clusters are shown in Figs. 8 and 9. In this preliminary analysis we have not taken into account the problem coming from the slightly different seeing of the u-band and V-band images. The measured colors may therefore be slightly affected by this atmospheric effect, in particular for the colors derived for the small apertures. In the present analysis the colors and magnitudes were measured within a fixed aperture radius of 10 pixels (2.13 arcsec, i.e. approximately 2 kpc for all clusters) from the center of each galaxy. We note that two clusters (A147 and MKW3s) have not yet been the subject of spectroscopic follow-up and so redshift information is not yet available.

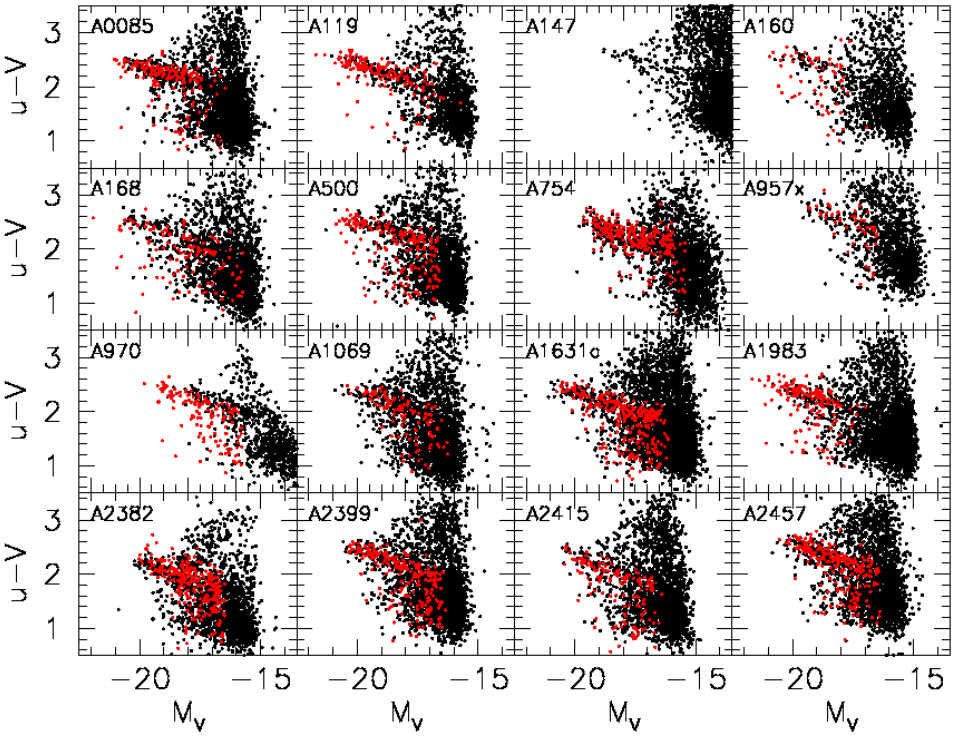

Fig. 8. $u - V$ color–magnitude diagrams of our clusters. The black dots mark the color of all galaxies in the fields, while the red dots mark the colours of galaxy members of the clusters according to their measured redshift.

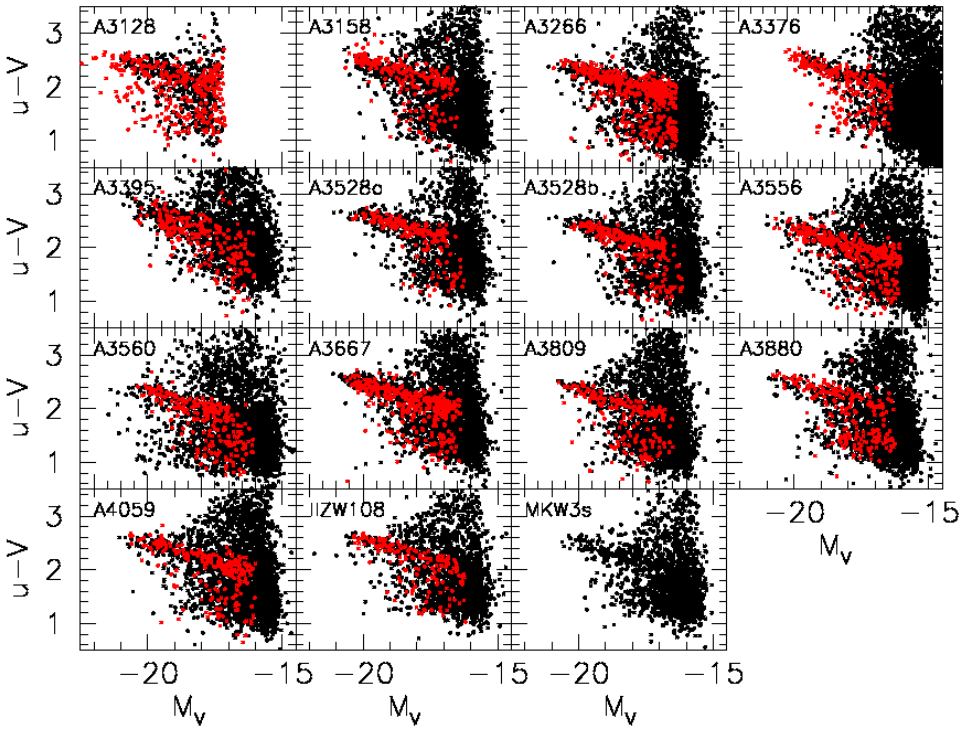

Fig. 9. $u - V$ CMDs of our clusters. Symbols are as in Fig. 8.

In general the presence of the red sequence is clearly visible in all diagrams. It is also clear that the most luminous galaxy members of the clusters are also the reddest ones. The mean $(u - V)$ color measured is around 2, but this value changes slightly according to the apertures used for the plot because of the effects of seeing and the occurrence of inner color gradients.

We isolated the region of the red sequence of the member galaxies and fitted the galaxy distribution. The fit excludes the sparse data with bluer colors that are clearly visible outside the red sequence. Figure 10 shows in red the area selected for the fit of the red sequence. We verified that the final fit coefficients do not depend on the choice of this area unless a substantial fraction of blue objects is included.

Table A.2 lists the coefficients of the fitted relation, the rms scatter, the correlation coefficient, and the number of points involved in the fit. The slope of the fits is similar for all clusters with an average value of -0.18 ± 0.03. The average scatter of the red sequence is small: 0.16 ± 0.03. This means that all clusters have a similar history with the same evolutionary processes at work. The age and the metallicity of the galaxies,

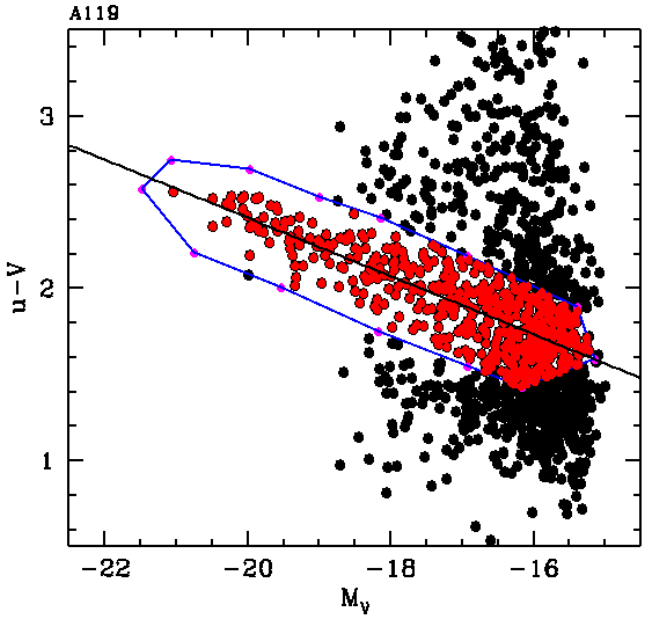

Fig. 10. $u - V$ color–magnitude diagrams of the cluster A119. The red dots mark the galaxies chosen for the fit of the red sequence.

which may affect the slope of the color–magnitude relation, are likely very similar everywhere. The observed homogeneity clearly explains why clusters are considered good cosmological tools.

For comparison, we remind the reader that the median slope of the $(B - V)$ versus M_V color magnitude diagrams was -0.047 ± 0.001 (Valentinuzzi et al. 2011). The slope of the red sequence in the u-band is therefore nearly a factor of five larger. However, here the M_V range of the red sequence used to obtain the slope is only of approximately 4 mag, while in the work of Valentinuzzi it was up to 2 mag larger (these latter authors used a Monte Carlo statistical field subtraction to obtain a better estimation of the red sequence at low magnitude level).

Another useful diagram that helps to understand cluster formation properties and the role played by the peculiar cluster environment is that showing how the color of galaxies changes with the distance from the brightest central galaxy (BCG) of the cluster. It is well known that many processes are at work to stop the star formation in such environments, causing important morphological transformations (see e.g., D'Onofrio et al. 2015).

Figure 11 presents the $u - V$ color of the galaxies that are members of the clusters as a function of the projected distance from the central BCG. The data have been binned in steps of 0.5 Mpc (black dots) and normalized to the mean color of the cluster A0085. This is done for graphical reasons in order to permit a better view of the spatial trends of the mean color of clusters. Using the same scale we can better appreciate the relative differences from cluster to cluster. The figure also lists in each box the maximum difference in color measured among the galaxies of the field. The clusters appearing in this figure are those having the information on the galaxy membership according to the WINGS database.

The general mean color trend is relatively constant from the center out to the periphery for all clusters, but we highlight the fact that the redder galaxies are preferentially situated in the central regions of the clusters, while the bluer galaxies are in the outer parts. However, the projected distribution of colors does not show a strong segregation of the red galaxies towards the cluster center, while instead the range spanned by the average color is similar in all clusters.

The homogeneity of the observed color distributions along the cluster extension seems to indicate again that in all clusters the evolution was dictated by the same processes. Both the star formation history of galaxies and the processes occurred inside the cluster fields were everywhere likely the same.

The maximum observed spread in color for the member galaxies is approximately two, indicating that our data include galaxies of the blue and red clumps of the CMD.

Figure 12 shows the $u - V$ color versus the stellar mass of the galaxies in log units. Here we use only cluster members. We highlight the fact that the galaxies where the star formation (SF) is stopped (SFR = 0) are essentially all along the red sequence, while those with ongoing SF (SFR $\neq$ 0) are distributed along a different, much steeper sequence. Notably, some objects are blue, but their measured SFR is equal to zero. These could be objects that have recently entered into the cluster environment.

In order to better check where these objects with SFR = 0 are situated in our clusters, Fig. 13 provides a histogram of the fraction of galaxies with measured SFR = 0 according to SINOPSIS (Fritz et al. 2007) at different cluster-centric distances. A total of 3472 galaxies are shown. We note that up to 10% of galaxies have SFR = 0 at a distance of ~2 Mpc. We also highlight the fact that there is a non-null fraction of galaxy members with no SF but with blue color even in the central region; 224 galaxies in total.

4.2. The SFR of galaxies as a function of absolute luminosity

The SFR is a key diagnostic parameter for understanding the evolution of galaxies across cosmic time. Star formation can be traced using several indicators at various wavelengths from X-rays to the radio domain (see e.g., Kennicutt 1998b; Hao et al. 2011; Zhou et al. 2017). The most used tracers are the UV continuum (directly linked to the photospheric emission of the young stellar component) and the IR emission (linked to the interstellar dust enshrouding the young stars re-emitting the absorbed UV flux). The u-band, being dominated by young stars, has been shown to be a relatively good SFR indicator (Cram et al. 1998; Hopkins et al. 2003, but see Sage & Solomon 1989 for an opposite claim), but a contribution from the old stellar population and a certain amount of dust extinction are disadvantages of this method. Nevertheless, Prescott et al. (2009) were able to estimate the SFH of galaxies using the u-band after removing such effects. In this context the present data allow us to understand to what extent the u-band photometry of galaxies can help to trace the SFH.

Figures 14 and 15 show how the current SFR in the galaxies changes with total luminosity. The SFR used here is that measured from the SED by Fritz et al. (2007) which is available from the WINGS database (the quantity named SFR1). This SFR represents the contribution coming from the stars born in the last 20 Myr and was derived using the program SINOPSIS realized by Fritz et al. (2007). The absolute magnitudes were instead derived using the total luminosities of the galaxies (given by MAG_AUTO) and the luminosity distances of the galaxies (also available from the WINGS database), after taking into account a K-correction term calculated on the basis of the redshift of each galaxy and its $(B - V)$ color. The data were corrected for galactic extinction, because this term, although different for the V and u-band, is constant for all galaxies of the same cluster. The net effect is therefore a small constant shift in the observed distributions.

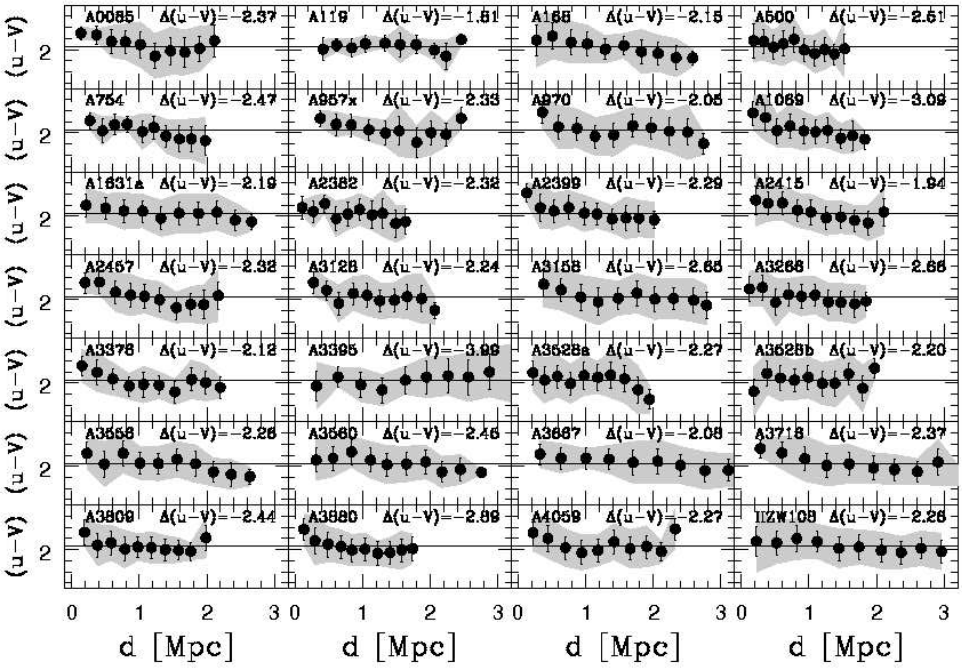

Fig. 11. $u - V$ color of galaxy members as a function of distance from the central BCG. The dots give the average value of the color in each bin. The gray area marks the semi inter-quartile range of the distribution.

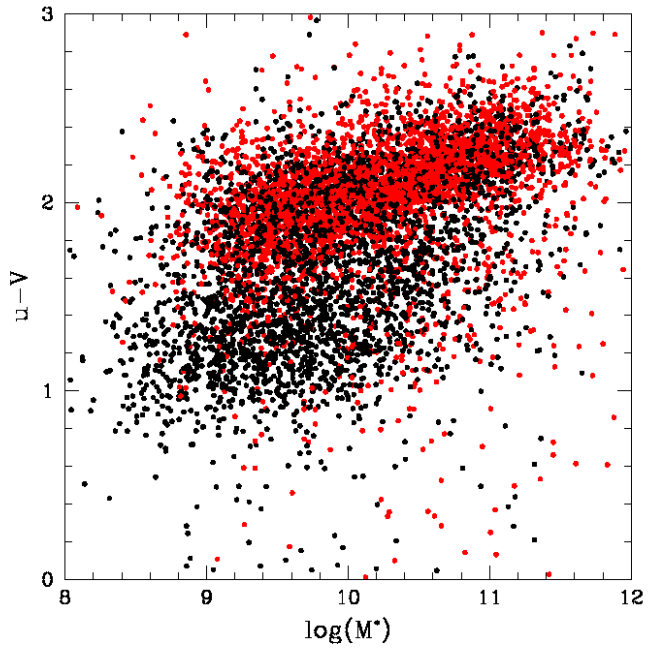

Fig. 12. $u - V$ color versus stellar mass of the galaxies in log units. The red dots mark the galaxies with measured SFR = 0, while the black dots those with SFR ≠ 0.

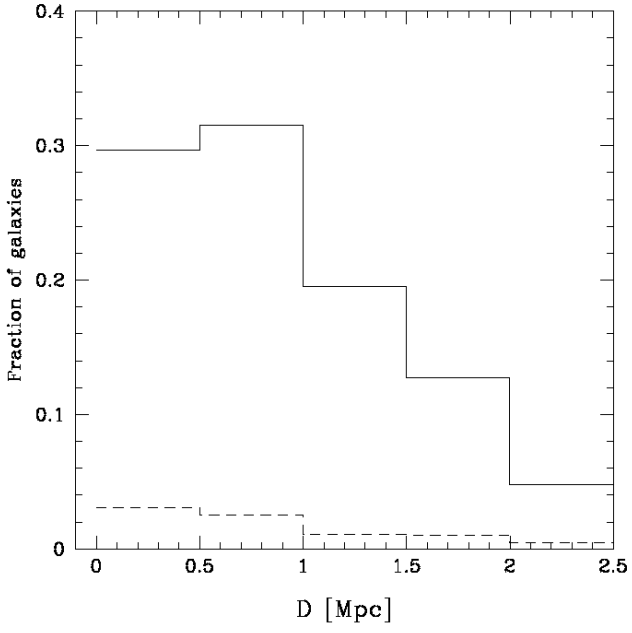

Fig. 13. Fraction of galaxies with SFR = 0 (solid line) at different cluster-centric distances. The measurement of the SFR = 0 is that provided by SINOPSIS (Fritz et al. 2007). The dashed line shows the same fraction but for the galaxies for which $u - V < 1.5$.

In both figures the red and black lines are the fits obtained by the program SLOPES (Feigelson & Babu 1992). The fit coefficients for Figs. 14 and 15 are listed in Table A.3. The same tables also provide the scatter around the fit and the number of galaxies involved. We note that the slopes of the fitted relations, which were obtained using SLOPES, are on average very similar for the V- and u-bands; they are identical within the errors. The average slope is -0.38 ± 0.04 (-0.40 ± 0.04) for the u-band (V-band). We also note that the few galaxies not belonging to the clusters follow the same distribution. These galaxies are not very far away; their redshift distribution peaks at $z \sim 0.1$ (Fraix-Burnet et al. 2019). The scatter is also very similar in all clusters, with an average value of ∼0.4.

Finally, we confirm that the SFR of the member galaxies of different morphological types follow the same trend with the projected cluster-centric distance showed by D'Onofrio et al. (2015, their Fig. 6). The conclusion that we draw from this raw analysis is that the u-band does not seems significantly better connected with the current SFR than the V-band. The V-band and the u-band are indeed substantially similar from this side. The effects of dust and the contribution of the old stellar population probably cannot be ignored at this redshift. Toward higher

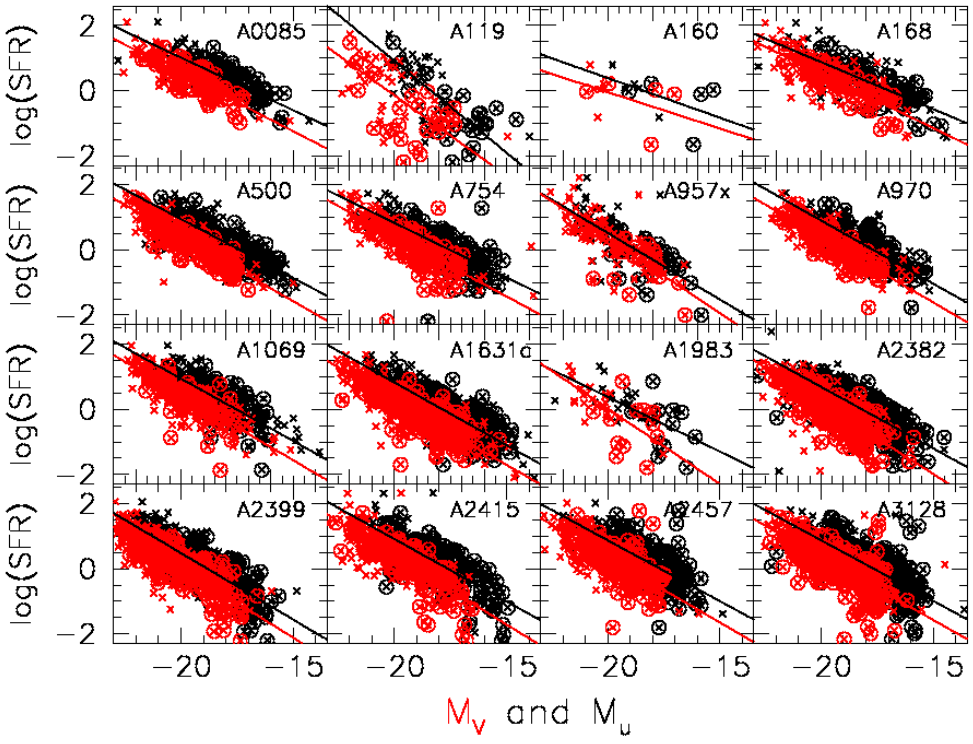

Fig. 14. SFR vs. the absolute magnitude of galaxies in the field of our clusters. The black cross dots mark the *u*-band data, while the red cross dots the *V*-band data. The circles surrounding the cross dots mark the galaxies that are member of the clusters according to their redshift.

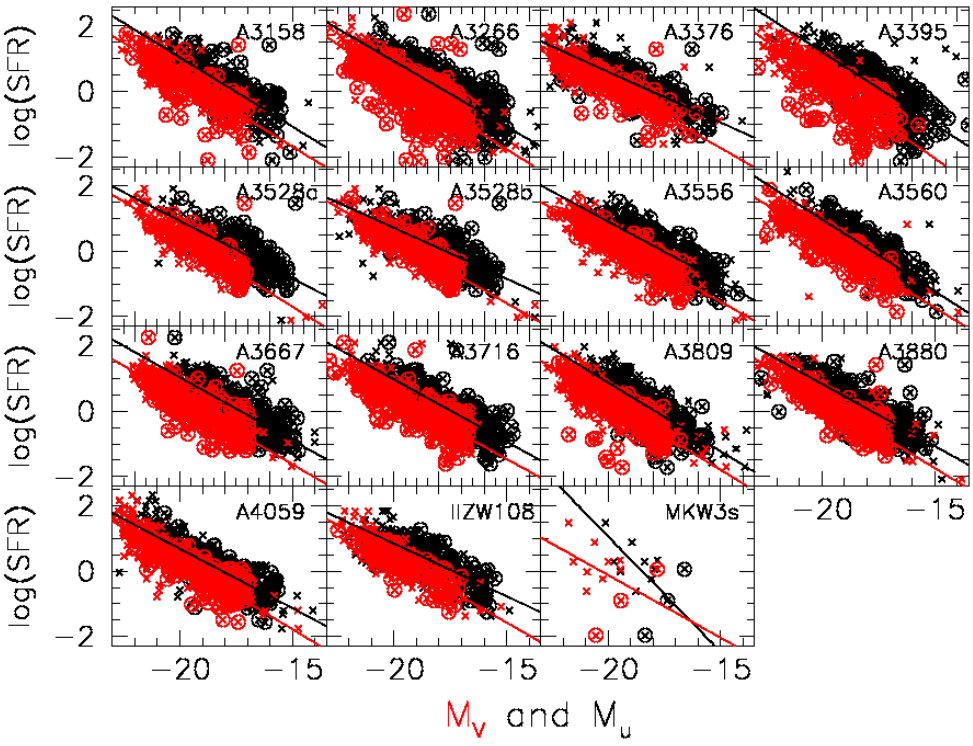

Fig. 15. SFR vs. the absolute magnitude of galaxies in the field of our clusters. The black cross dots mark the *u*-band data, while the red cross dots the *V*-band data. The circles surrounding the cross dots mark the galaxies that are member of the clusters according to their redshift.

redshifts, the contribution of the young stellar population should likely dominate, making the *u*-band the most robust tracer of SFR.

5. Conclusions

Here, we present photometric catalogs obtained with a `SExtractor` analysis of 39 clusters of the WINGS survey imaged using the VST telescope in the *u*-band. The main steps of the data reduction and calibration are described, showing in particular a comparison between the previous *u*-band extension of WINGS and that with the *u*-band SDSS photometry. The catalogs are available at the CDS in Strasbourg.

We also show some examples of the possible uses of these data, presenting CMDs of the observed clusters, the color–mass relation, the projected spatial distribution of galaxy colors, and the correlation of the *u* and *V* luminosities with the current SFR of galaxies previously derived from the spectral analysis.

These data suggest substantial homogeneity in galaxy SFH and cluster evolution for the 39 clusters studied here. The CMDs are relatively similar in slope and scatter, the spatial color distribution is approximately equal and constant in all clusters, and the current SFR correlates with the *u*-band and *V*-band luminosities in the same way. The red sequence is also clearly visible in the stellar mass–color relation and appears to be formed in particular by the galaxies where the SF is stopped.

In conclusion, our analysis suggests that clusters are good cosmological probes, and therefore it is important to follow their evolution back in time.

Acknowledgements. MD wants to acknowledge ESO for the data of this GTO survey.

References

Alam, S., Albareti, F. D., & Allende Prieto, C. 2015, ApJS, 219, 27
Barbaro, G., & Poggianti, B. M. 1997, A&A, 324, 490
Bertin, E. 2006, in Astronomical Data Analysis Software and Systems XV, eds. C. Gabriel, C. Arviset, & D. Ponz, et al., ASP Conf. Ser., 351, 112
Bertin, E., & Arnouts, S. 1996, A&AS, 117, 393
Bertin, E., Mellier, Y., Radovich, M., et al. 2002, in Astronomical Data Analysis Software and Systems XI, eds. D. A. Bohlender, D. Durand, & T. H. Handley, ASP Conf. Ser., 281, 228
Bower, R. G., Lucey, J. R., & Ellis, R. S. 1992, MNRAS, 254, 601
Bower, R. G., Kodama, T., & Terlevich, A. 1998, MNRAS, 299, 1193
Capaccioli, M., Spavone, M., Grado, A., et al. 2015, A&A, 581, A10
Cariddi, S., D'Onofrio, M., Fasano, G., et al. 2018, A&A, 609, A133
Cava, A., Bettoni, D., & Poggianti, B. M. 2009, A&A, 495, 707
Cram, L., Hopkins, A., Mobasher, B., et al. 1998, ApJ, 507, 155
D'Onofrio, M., Marziani, P., & Buson, L. 2015, Front. Astron. Space Sci., 2, 4
Fasano, G., Marmo, C., Varela, J., et al. 2006, A&A, 445, 805
Fasano, G., Vanzella, E., Dressler, A., et al. 2012, MNRAS, 420, 926
Feigelson, E. D., & Babu, G. J. 1992, ApJ, 397, 55
Fraix-Burnet, D., D'Onofrio, M., & Marziani, P. 2019, A&A, 630, A63
Fritz, J., Poggianti, B. M., Bettoni, D., et al. 2007, A&A, 470, 137
Fritz, J., Poggianti, B. M., Cava, A., et al. 2011, A&A, 526, A45
Grado, A., Capaccioli, M., Limatola, L., & Getman, F. 2012, Mem. Soc. Astron. It. Suppl., 19, 362
Gullieuszik, M., Poggianti, B. M., Fasano, G., et al. 2015, A&A, 581, A41
Hao, C. N., Kennicutt, R. C., Johnson, B. D., et al. 2011, ApJ, 741, 124
Hopkins, A. M., Miller, C. J., Nichol, R. C., et al. 2003, ApJ, 599, 971
Kennicutt, R. C. 1998a, ApJ, 498, 541
Kennicutt, R. C. 1998b, ARA&A, 36, 189
Landolt, A. U. 1992, AJ, 104, 340
Moretti, A., Poggianti, B. M., Fasano, G., et al. 2014, A&A, 564, A138
Moretti, A., Gullieuszik, M., Poggianti, B. M., et al. 2017, A&A, 599, A81
Omizzolo, A., Fasano, G., Reverte Paya, D., et al. 2014, A&A, 561, A111
Prescott, M., Baldry, I. K., & James, P. A. 2009, MNRAS, 397, 90
Sage, L. J., & Solomon, P. M. 1989, ApJ, 342, L15
Sciarratta, M., Chiosi, C., D'Onofrio, M., & Cariddi, S. 2019, ApJ, 870, 70
Skrutskie, M. F., Cutri, R. M., Stiening, R., et al. 2006, AJ, 131, 1163
Tully, R. B., Mould, J. R., & Aaronson, M. 1982, ApJ, 257, 527
Valentinuzzi, T., Woods, D., Fasano, G., et al. 2009, A&A, 501, 851
Valentinuzzi, T., Poggianti, B. M., Fasano, G., et al. 2011, A&A, 536, A34
Varela, J., D'Onofrio, M., Marmo, C., et al. 2009, A&A, 497, 667
Zhou, Z., Zhou, X., Wu, H., et al. 2017, ApJ, 835, 70

Appendix A: Results of the fits of the color–magnitude relations and of the log(SFR)–*M* relations

Table A.1 provides a glance at the data that can be downloaded from the CDS in Strasbourg. We show for graphical reasons only the first six columns and rows for cluster A0085.

In the other two tables we provide the results of the least square fits obtained using the program SLOPES on the red sequence of the CMD and on the log(SFR)−*M* distribution of galaxies in the *V* and *u*-bands.

Table A.1. Example of the catalogs with the `SExtractor` photometry in the *u*-band for cluster A85 downloadable from the CDS.

WINGS_ID	CLUSTER	RA	Dec	X_PEAK	Y_PEAK	...
WINGSJ004253.82−095051.5	A85	10.724256565	−9.847632733	14682	148	...
WINGSJ004324.04−095055.2	A85	10.850178927	−9.848668809	16775	128	...
WINGSJ004242.55−095053.9	A85	10.677286989	−9.848296374	13902	138	...
WINGSJ004238.11−095101.9	A85	10.658777144	−9.850536162	13594	100	...
WINGSJ004151.90−095101.0	A85	10.466261266	−9.850277102	10394	106	...
...	...	...	...	...	...	...

Table A.2. Slopes and intercepts of the color–magnitude relations for our clusters.

Cluster	SLOPE	INTERCEPT	RMS	CORR. COEF.	N_GAL
A0085	−0.16	−0.86	0.11	−0.89	810
A119	−0.21	−1.77	0.15	−0.87	605
A147	−0.19	−1.36	0.26	−0.63	156
A160	−0.21	−1.58	0.14	−0.85	497
A168	−0.25	−2.34	0.20	−0.81	1144
A500	−0.26	−2.62	0.17	−0.84	836
A754	−0.15	−1.72	0.11	−0.87	596
A957x	−0.15	−1.79	0.15	−0.73	423
A1069	−0.18	−1.28	0.15	−0.81	668
A1631a	−0.20	−1.67	0.16	−0.84	1481
A1983	−0.20	−1.68	0.16	−0.83	1023
A2382	−0.20	−1.87	0.17	−0.81	741
A2399	−0.19	−1.40	0.16	−0.81	887
A2415	−0.20	−1.59	0.16	−0.80	747
A2457	−0.18	−1.00	0.14	−0.84	699
A3128	−0.17	−0.90	0.14	−0.73	305
A3158	−0.18	−1.18	0.18	−0.76	1013
A3266	−0.14	−0.90	0.14	−0.81	1215
A3376	−0.20	−2.10	0.18	−0.78	1024
A3395	−0.20	−1.20	0.20	−0.77	1332
A3528a	−0.16	−0.70	0.15	−0.80	782
A3528b	−0.14	−0.50	0.11	−0.85	730
A3556	−0.16	−0.80	0.17	−0.77	1131
A3560	−0.19	−1.50	0.20	−0.75	1235
A3667	−0.16	−0.67	0.14	−0.82	1152
A3809	−0.18	−1.24	0.17	−0.74	819
A3880	−0.18	−1.27	0.18	−0.76	897
A4059	−0.17	−0.87	0.19	−0.70	1299
IIZW108	−0.19	−1.36	0.18	−0.74	836
MKW3s	−0.18	−1.22	0.17	−0.79	750

Table A.3. Slopes and intercepts of the log(SFR)−*M* relations for our clusters.

Cluster	SLOPE	E_SLOPE	INTERCEPT	E_INTERCEPT	N_GAL	RMS	BAND
A0085	−0.324	0.027	−5.473	0.498	157	0.332	*u*
A0085	−0.355	0.023	−6.584	0.463	157	0.327	*V*
A119	−0.565	0.078	−10.40	1.379	61	0.68	*u*
A119	−0.495	0.083	−10.05	1.651	61	0.766	*V*
A160	−0.244	0.16	−4.502	2.768	11	0.515	*u*
A160	−0.225	0.201	−4.552	3.862	11	0.555	*V*
A168	−0.29	0.026	−4.929	0.473	199	0.383	*u*
A168	−0.334	0.023	−6.171	0.440	199	0.366	*V*
A500	−0.363	0.019	−6.317	0.357	349	0.366	*u*
A500	−0.395	0.019	−7.510	0.374	349	0.318	*V*
A754	−0.336	0.029	−5.897	0.515	213	0.43	*u*
A754	−0.371	0.031	−7.003	0.585	213	0.419	*V*
A957x	−0.410	0.049	−7.684	0.788	124	0.507	*u*
A957x	−0.460	0.037	−8.852	0.738	124	0.487	*V*
A970	−0.389	0.017	−6.880	0.318	241	0.359	*u*
A970	−0.402	0.018	−7.652	0.358	241	0.333	*V*
A1069	−0.383	0.017	−6.724	0.310	335	0.364	*u*
A1069	−0.404	0.017	−7.633	0.333	335	0.351	*V*
A1631a	−0.386	0.015	−6.899	0.267	500	0.401	*u*
A1631a	−0.400	0.016	−7.713	0.306	500	0.405	*V*
A1983	−0.336	0.081	−6.343	1.520	36	0.539	*u*
A1983	−0.464	0.093	−9.262	1.813	36	0.538	*V*
A2382	−0.379	0.022	−6.895	0.408	451	0.431	*u*
A2382	−0.438	0.018	−8.568	0.346	451	0.406	*V*
A2399	−0.409	0.015	−7.706	0.290	534	0.394	*u*
A2399	−0.431	0.016	−8.593	0.319	534	0.388	*V*
A2415	−0.384	0.030	−6.773	0.551	324	0.477	*u*
A2415	−0.424	0.024	−8.084	0.484	324	0.438	*V*
A2457	−0.374	0.018	−6.613	0.335	335	0.421	*u*
A2457	−0.402	0.019	−7.691	0.373	335	0.415	*V*
A3128	−0.373	0.02	−6.590	0.361	461	0.448	*u*
A3128	−0.388	0.019	−7.405	0.355	461	0.437	*V*
A3158	−0.424	0.022	−7.450	0.390	370	0.432	*u*
A3158	−0.424	0.021	−8.062	0.408	370	0.431	*V*
A3266	−0.400	0.026	−7.087	0.471	648	0.490	*u*
A3266	−0.430	0.018	−8.235	0.339	648	0.492	*V*
A3376	−0.311	0.020	−5.625	0.393	340	0.459	*u*
A3376	−0.393	0.022	−7.640	0.434	340	0.408	*V*
A3395	−0.444	0.031	−7.681	0.534	323	0.572	*u*
A3395	−0.482	0.023	−9.292	0.451	323	0.522	*V*
A3528a	−0.353	0.030	−6.138	0.536	229	0.438	*u*
A3528a	−0.429	0.019	−8.143	0.367	229	0.355	*V*
A3528b	−0.312	0.022	−5.530	0.403	314	0.415	*u*
A3528b	−0.391	0.014	−7.460	0.274	314	0.335	*V*
A3556	−0.371	0.012	−6.514	0.209	419	0.343	*u*
A3556	−0.383	0.011	−7.301	0.212	419	0.332	*V*
A3560	−0.440	0.021	−7.832	0.373	369	0.382	*u*
A3560	−0.422	0.020	−8.064	0.381	369	0.374	*V*
A3667	−0.386	0.014	−6.691	0.242	404	0.386	*u*
A3667	−0.403	0.015	−7.683	0.297	404	0.382	*V*
A3716	−0.381	0.015	−6.655	0.273	348	0.407	*u*
A3716	−0.381	0.015	−7.186	0.297	348	0.414	*V*
A3809	−0.421	0.013	−7.551	0.237	615	0.337	*u*
A3809	−0.419	0.013	−8.094	0.267	615	0.346	*V*
A3880	−0.381	0.022	−6.791	0.402	415	0.391	*u*
A3880	−0.419	0.014	−8.035	0.279	415	0.325	*V*
A4059	−0.364	0.014	−6.603	0.273	505	0.39	*u*
A4059	−0.414	0.013	−8.000	0.263	505	0.363	*V*
IIZW108	−0.322	0.026	−5.606	0.484	343	0.388	*u*
IIZW108	−0.397	0.017	−7.537	0.342	343	0.332	*V*
MKW3s	−0.708	0.484	−13.10	8.793	12	0.761	*u*
MKW3s	−0.385	0.543	−7.826	10.94	12	0.818	*V*
AVERAGE	−0.38	0.04	−6.88	0.81		0.44	*u*
AVERAGE	−0.40	0.04	−7.80	0.91		0.42	*V*